

# III-V photonic crystal wire cavity laser on silicon wafer

Yacine Halioua,<sup>1,2,\*</sup> Alexandre Bazin,<sup>1</sup> Paul Monnier,<sup>1</sup> Timothy J. Karle,<sup>1</sup> Isabelle Sagnes,<sup>1</sup> Gunther Roelkens,<sup>2</sup> Dries Van Thourhout,<sup>2</sup> Fabrice Raineri,<sup>1,3</sup> and Rama Raj<sup>1</sup>

<sup>1</sup>Laboratoire de Photonique et de Nanostructures, CNRS-UPR20, Route de Nozay, 91460 Marcoussis, France

<sup>2</sup>Photonics Research Group, Department of Information Technology, Ghent University, B-9000 Ghent, Belgium

<sup>3</sup>Université Paris Denis Diderot, 75205 Paris, France

\*Corresponding author: yacine.halioua@lpn.cnrs.fr

Received April 26, 2010; revised August 12, 2010; accepted August 18, 2010;  
posted August 18, 2010 (Doc. ID 127606); published September 29, 2010

We report on the modeling and experimental characterization of an InP-based photonic crystal wire cavity laser bonded to a silicon wafer. Simulations give an insight into the variation of the resonant mode frequency and the dependence of the  $Q$ -factor on the geometrical parameters of the laser cavity. Calculated and measured  $Q$ -factors are of the order of  $10^4$ . A low threshold laser operation is demonstrated. © 2010 Optical Society of America

OCIS codes: 350.4238, 140.3460, 130.3120.

## 1. INTRODUCTION

Heterogeneous integration of III-V semiconductor devices on silicon has gained considerable momentum in the last few years due to the drive toward obtaining laser sources in a complementary metal-oxide semiconductor compatible platform [1,2]. The introduction of nanolasers, such as photonic crystal (PhC) III-V semiconductor lasers [3], would enable high speed operation [4,5] and reduced power consumption [6] with considerable reduction in footprint. The integration of PhC lasers onto silicon has recently been demonstrated using different wafer bonding techniques such as SiO<sub>2</sub>-SiO<sub>2</sub> molecular bonding [7], Au-In eutectic bonding [8], or adhesive bonding [9]. In all these structures, the PhC slab is separated from the Si substrate by a low-refractive index (low- $n$ ) silicon dioxide (SiO<sub>2</sub>) or benzo-cyclo-butene (BCB) polymer layer for the vertical confinement of light. The presence of this layer reduces the optical confinement (compared to an air-clad membrane) making it less straightforward to obtain high  $Q$  (quality factor) cavities, such as those demonstrated in suspended membranes [10]. This is one of the reasons why previously demonstrated lasers rely principally upon low-group velocity modes either at a band edge [7,8] or at a waveguide mode edge [11,12].

In this work, we report on the simulation and fabrication of active InP-based PhC wire nanocavity lasers bonded to a silicon wafer (see Fig. 1). These small volume,  $V$ , defect cavities consist of a single-mode wire waveguide with mirrors formed by drilling a row of holes along the wire at either end [13], enabling record of high  $Q/V$  ratios, even in the case where the substrate is a low- $n$  layer such as silica. The cavity mode is confined close to the center of the photonic bandgap. So far these defect structures have been made in passive materials such as Si [14,15]. Recently band edge nanobeam lasers have been demonstrated using air-bridge structures [16–18] in

GaAs- and InP-based materials, where the cavity is formed by a continual tapering of the holes. This confines the propagating band edge modes of the central portion of the cavity with the weakly evanescent modes at the band edge of the mirror [19]. All of these cavities should be excellent candidates for enhancing nonlinear effects including gain. In order to explore the possibilities that our defect cavities offer for laser emission, we study both numerically and experimentally their performance by varying their geometrical parameters. Particular attention is given to the length of the cavity as it determines the resonance wavelength and the quality factor. The close matching between the expected and observed results attest to the fine tuned simulation and the accuracy of the fabrication, both of which lead finally to the demonstration of an efficient low threshold laser operation.

## 2. DESIGN AND MODELING OF THE WIRE CAVITIES

The cavities under investigation are made in a 550 nm wide 255 nm thick InP strip waveguide incorporating four InGaAs/InGaAsP quantum wells (QWs) as an active medium. Two sets of holes are drilled along the waveguide to form the high reflectivity mirrors, spaced by a gap of length  $L$  to form a cavity. The length  $L$  is varied to obtain different cavity lengths. Each high reflectivity mirror is made of 11 holes with a periodic section of eight holes plus three holes with gradually decreasing diameters to form a taper which is situated at the edge of the cavity defect zone. Laterally, light is confined within the cavity by index guiding due to the semiconductor/air interface, and in the vertical direction by air above and BCB below. Our wire cavity structure is bonded to an unpatterned silicon wafer by a transparent 1  $\mu$ m thick low index BCB joint layer ( $n=1.54$  at 1.55  $\mu$ m). The schematics are given in Fig. 1.

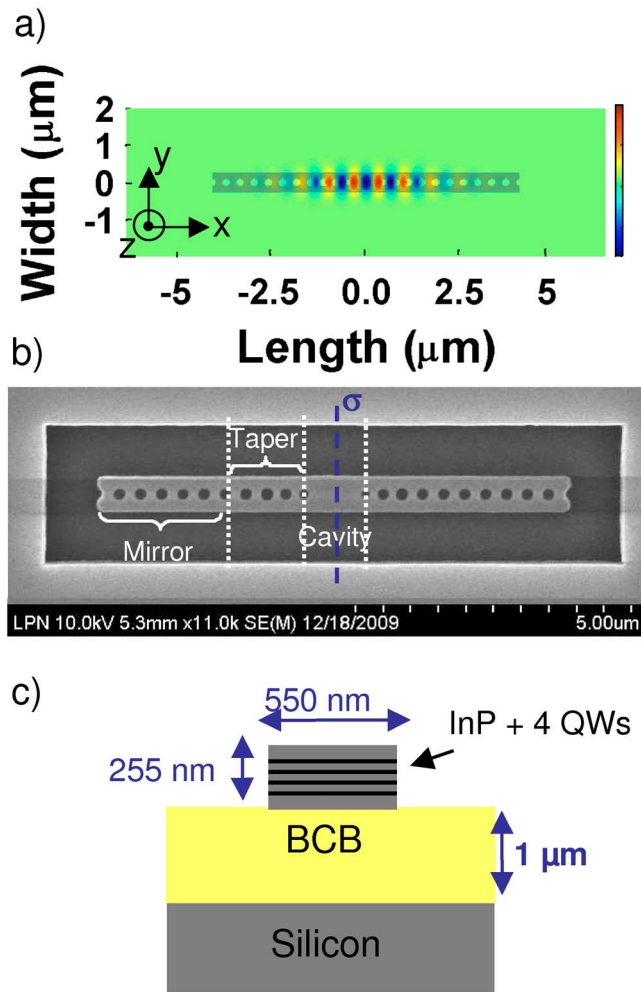


Fig. 1. (Color online) (a)  $E_y$  field for the second order symmetric mode. (b) SEM image of the sample. The thick dotted line denotes the symmetry axis ( $\sigma_x$ ) taken for the cavity mode. (c) Schematic of the vertical heterostructure.

The resonance wavelength is determined by several parameters: the length of the cavity, the effective index of the mode confined in the wire, and the phase change induced by the mirror reflection. In these kinds of structures it has been shown that high  $Q$  values may be obtained by tapering the size of the first three holes on either side of the cavity [20]. The tapering is designed to adiabatically minimize the modal mismatch between the propagating guided mode and the evanescent mirror modes, thereby decreasing the losses at the cavity/mirror interface and thus increasing the reflectivity.

We optimize our structure using three-dimensional finite-difference time domain (3D FDTD) simulation [21], starting with a cavity design which has already been demonstrated to possess a high  $Q$  in the silicon-on-insulator material system [14]. The design is pertinently modified in order to incorporate all the relevant material and geometrical parameters of our desired InP-based structure. By iterating the radius and period that give the largest bandgap and therefore the best confinement, we designed the wire cavity lattices in the InP-based system. We align the center of the mirror's high reflectivity response with the wavelength ( $\lambda = 1.55 \mu\text{m}$ ) where maximum gain is available from our active layer. From the simulation for the periodic section of the mirror zone, we

obtain a period of 376 nm and a hole radius of 97 nm. For the tapered-hole section of the mirror we space the holes by 376.5, 337, and 320 nm and decrease their radii to 99, 85.5, and 69 nm, respectively [the fabricated structure is shown in Fig. 1(b)].

We then calculate, as a function of the cavity length, the four essential parameters: the resonant wavelengths, the  $Q$  factor, the modal volume, and the confinement factor. The resonant wavelengths are plotted in Fig. 2

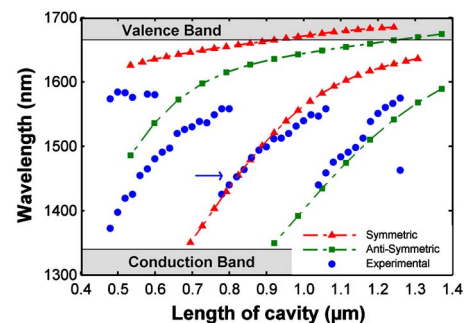


Fig. 2. (Color online) Resonance wavelength plotted against cavity length. 3D FDTD simulation results are joined by dashed lines, and the dots show the corresponding experimental measurements. Arrow points to the second order symmetric mode.

against the cavity length. Two orders of the Fabry–Perot (FP) modes for the symmetric (triangles) and antisymmetric (squares) modes are represented (see the symmetry axis shown in Fig. 1). The dispersion ( $d\lambda/dL$ , where  $L$  is the length of the cavity) is mostly due to the wavelength dependent variation of the penetration depth into the mirrors as confirmed from two-dimensional simulations (not shown here). The FP resonator behavior is observed; below 1555 nm, the resonance wavelength of the cavity shifts steeply and linearly to higher values with increasing cavity length (large  $d\lambda/dL$ ). Closer to the valence band edge of the mirrors the gradient becomes gradually shallower (small  $d\lambda/dL$ ), and varying the length has little effect on the wavelength: here the field is weakly confined in the defect and leaks through the mirrors. [The field is quasi-transverse-electric, and we obtain modes which are both symmetric and antisymmetric with respect to reflection in the  $y$ - $z$  plane ( $\sigma_x$  as shown in Fig. 1).] Further, no FP modes are seen for wavelengths less than 1360 nm as they fall outside the PhC bandgap, and also the limit of total internal reflection in the mirrors.

In Fig. 3(a) we plot with triangles the simulated  $Q$  factor versus the cavity length corresponding to the symmet-

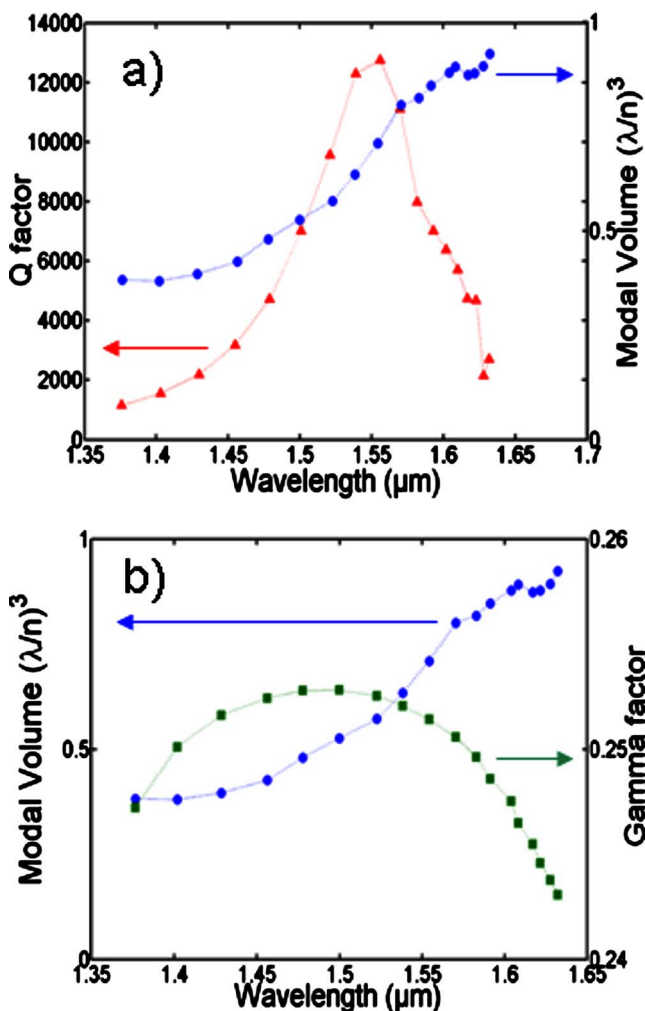


Fig. 3. (Color online) (a)  $Q$  factor and modal volume extracted from the 3D FDTD simulations as a function of the resonance wavelength. (b) Modal volume and confinement factor as functions of the resonance wavelength.

ric mode indicated by the arrow in Fig. 2. It is seen, for the second order symmetric mode, that  $Q$  attains, in our system, a maximum of  $1.3 \times 10^4$  for a cavity length of 1  $\mu\text{m}$ , giving a resonance at 1556 nm. We expect that the maximum  $Q$  factor is reached when the tapered mirror reflectivity is a maximum. As indicated in [20] this is found at wavelengths where the best modal matching between the cavity and the mirror modes is obtained thanks to the tapered zone, thereby fixing the cavity lengths that give the best  $Q$  factor. The  $Q$ -curve shows a smooth rise for shorter wavelengths, whereas it falls off rather abruptly for longer wavelengths as the wavelength associated with the highest  $Q$  cavity mode is closer to the valence band edge of the mirrors as can be seen in Fig. 2. We also calculate the modal volume [22] of the cavities using 3D FDTD and plot it as a function of the resonant wavelength in Fig. 3(a) (dots) and as a function of the cavity length in Fig. 3(b) (dots). We obtain modal volumes ranging from 0.38 to  $0.92(\lambda/n)^3$  for cavities lengths of 0.7  $\mu\text{m}$  ( $\lambda=1351$  nm) to 1.3  $\mu\text{m}$  ( $\lambda=1636$  nm). The volume increases rapidly with the length and the wavelength up to  $L=1.05$   $\mu\text{m}$  and is then almost constant for  $L>1.05$   $\mu\text{m}$ . Finally, we calculate the confinement factor,  $\Gamma$  which is defined as the ratio of the electric field energy density confined in the semiconductor active material (here the four InGaAs QWs whose dimensions are given in Section 3) to the total electric field energy density stored in the mode. This parameter is important when laser emission is considered, as only the field overlapping the active material is directly amplified. As seen in Fig. 3(b) (squares),  $\Gamma$  varies from 0.243 to 0.252, meaning that only a variation of 3% is obtained for the whole set of cavities. From Figs. 3(a) and 3(b), it is seen that the maximum in  $Q$  and mode confinement are obtained for the same modal volume.

### 3. FABRICATION AND OPTICAL CHARACTERIZATION

The fabricated structure consists of a 255 nm thick InP-based membrane bonded on an unpatterned silicon wafer using a 1  $\mu\text{m}$  thick layer of BCB ( $n=1.54$ ) [23]. The InP heterostructure incorporating four InGaAs/InGaAsP QWs (of thickness 13.5 nm/16 nm, respectively) grown by metal-organic chemical-vapor deposition exhibits photoluminescence (PL) that peaks around 1.55  $\mu\text{m}$  [see Fig. 4(c)]. The wire cavity is obtained using electron beam lithography followed by plasma etching [12]. Details of the etching may be found in [24]. As can be seen from the scanning electron microscope (SEM) image in Fig. 1, the wire cavity is isolated from the rest of the InP-based slab by a 1  $\mu\text{m}$  wide air trench. The cavity length is varied between 465 and 1465 nm in steps of 25 nm in order to obtain resonances over the full range of the QW gain.

We explore the fabricated samples at room temperature by measuring the light emitted under optical pumping. The samples are surface pumped using a  $50\times$  IR long working distance objective which focuses the pump light down to a spot size around 1.5  $\mu\text{m}$ . The laser source for the pump is a diode laser at 808 nm modulated to produce 10 ns pulses at 333 kHz repetition rate. These characteristics are chosen so as to reduce device heating. The near-

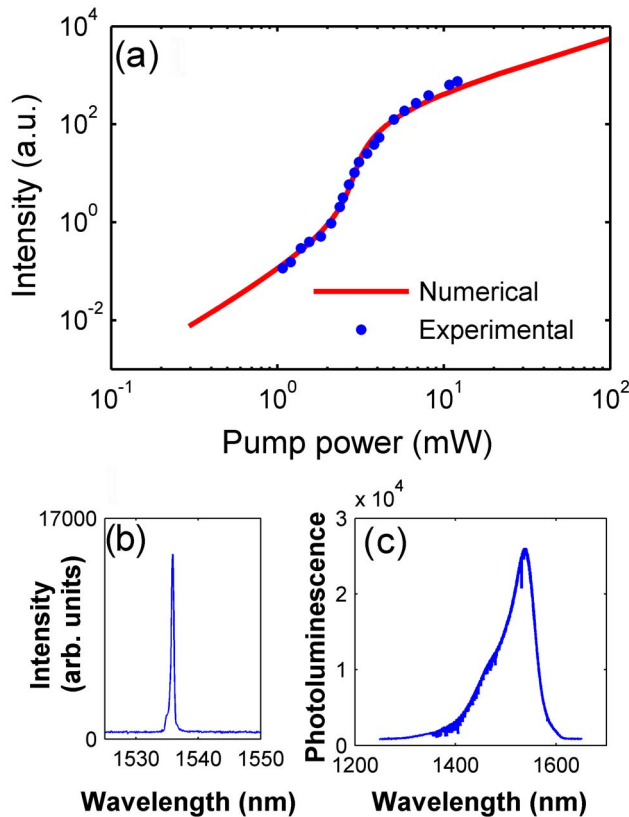


Fig. 4. (Color online) (a) Measured threshold and corresponding fitted rate equation versus pump power. (b) Spectrum under lasing operation. (c) PL spectrum of the QWs.

infrared pump is absorbed by all of the semiconductor materials, Si, InP, InGaAs QWs, and their InGaAsP barriers. The light emission is collected by the same objective, separated from the pump by a dichroic mirror and is analyzed using a spectrometer equipped with a cooled InGaAs photodiode array.

For each cavity, the wavelength of the peaks observed in the PL spectra is plotted in Fig. 2 with dots, as a function of the cavity length. Resonances are observed over the entire QW gain bandwidth, i.e., from 1373 to 1575 nm. The experimental measurements agree very well with the simulated predictions. We see that for cavities with lengths between 0.78 and 1.05  $\mu\text{m}$  the experimental results closely follow the  $d\lambda/dL$  trend from simulation. For longer cavities, the resonant wavelengths also follow the simulated cavity mode dispersion closely. For very short cavities, however, there is a shift in the curve arising from very slight changes in the radii of the holes due to electron beam lithography proximity effects that are stronger when the two mirrors are closer.

Laser operation is obtained over a wide range of wavelengths with a threshold ranging from 1 mW to 7.8 mW peak power (total input power incident upon the sample). As an example of laser operation, we plot in Fig. 4 the variation of the emitted power (circles) as a function of the pump peak power on a log-log scale for one cavity (cavity length=920 nm, 1535 nm lasing wavelength). We observe the typical S-shape attesting to the transition from spontaneous emission to stimulated emission [25], at 3.4 mW of peak pump power. These measurements are

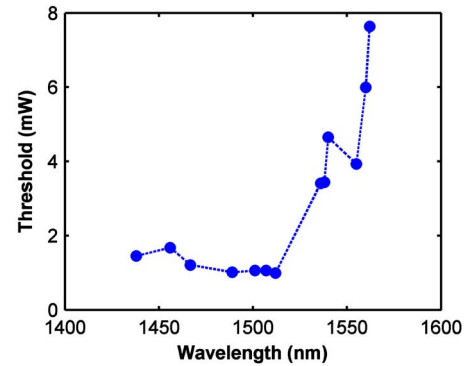


Fig. 5. (Color online) Threshold of the studied cavities plotted as a function of the emission wavelength.

performed for each of the cavities in order to deduce the corresponding threshold peak pump powers. The measurements correspond to the second order longitudinally symmetric mode; the third set of experimental points is identified by an arrow in Fig. 2. This is done in two steps. First is by solving the rate equations for QW lasers [5] by injecting the known values for the differential gain ( $3 \times 10^{-16} \text{ cm}^{-2}$ ), confinement factor (0.25), carrier density at transparency ( $2 \times 10^{18} \text{ cm}^{-3}$ ), carrier lifetime (200 ps), and the group velocity ( $10^{10} \text{ cm s}^{-1}$ ). Then the S-curves are fitted by varying the photon lifetime  $\tau_p$  and the fraction of the spontaneous emission rate captured by the laser mode,  $\beta$ , which are different for each cavity. From the fits we extract the thresholds (see Fig. 5) for each cavity using the condition that at the threshold for laser emission the photon density is equal to 1 [26]. The laser threshold diminishes slowly as the cavity emission shifts from 1437 nm (cavity length=0.8  $\mu\text{m}$ ) up to 1515 nm for a cavity length of 0.94  $\mu\text{m}$ , hitting a minimum threshold peak power of 1 mW. Then, as the cavity mode goes beyond 1539 nm (cavity length > 1  $\mu\text{m}$ ), the thresholds increase sharply.

#### 4. DISCUSSION AND CONCLUSIONS

In order to establish a relationship between the  $Q$  factor and the optimal operation of these lasers,  $\tau_p$ 's obtained from the rate equation fit are compared to the  $Q$  factors ( $Q = \tau_p \omega / 2$ ) obtained by modeling. These  $Q$  values are plotted in Fig. 6, showing that whereas the calculated  $Q$  factors reach a maximum value of  $1.3 \times 10^4$ , the experimental values peak at  $8 \times 10^3$ . The two data sets corre-

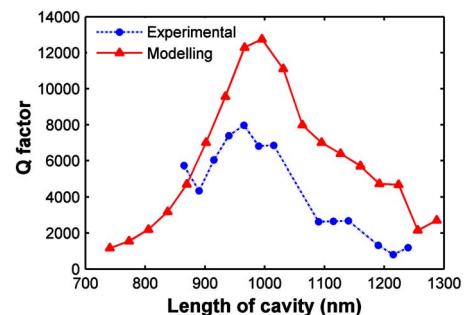


Fig. 6. (Color online) Experimental  $Q$  factors and modeled  $Q$  factors as functions of cavity length.

spond very well, with the slightly lower values obtained in the experiment attributable to fabrication roughness. The initially smooth increase for shorter wavelengths is due to the fact that the modes are well confined in the “deepest” position of the gap, whereas on the longer wavelength side the sharply decreasing  $Q$  is due to the fact that the mode is now located to close to the valence band and is no longer well confined.

In conclusion, we have demonstrated lasing operation with a fairly low threshold of InP-based wire cavity structures on a silicon substrate over a wavelength range from 1437 to 1565 nm. The influence of the cavity length upon the resonant wavelength, the  $Q$  factor, the modal volume, and the confinement factor was meticulously analyzed both numerically and experimentally. Our results show that an optimal value for the cavity length can be found to obtain the lowest laser threshold. Moreover, the close correspondence between the experimental measurements and the numerical calculations illustrates the quality and the accuracy of the technological processing. The results are a clear demonstration that III-V wire cavities are excellent candidates for ultracompact ( $\mu\text{m}^2$  scale footprint) building blocks in active nanophotonics on silicon, as it is possible to obtain high  $Q$  factors in such a substrate based hybrid system possessing both mechanical and thermal stabilities.

## ACKNOWLEDGMENTS

We thank R. Braive for the etching of the photonic crystals and F. Bordas for useful discussions. This work was partly funded by FP7 ICT European project HISTORIC and ANR jeunes chercheurs PROWOC.

## REFERENCES

1. A. W. Fang, H. Park, Y. Kuo, R. Jones, O. Cohen, D. Liang, O. Raday, M. N. Sysak, M. J. Paniccia, and J. E. Bowers, “Hybrid evanescent silicon devices,” *Mater. Today* **10**, 28–35 (2007).
2. J. Van Campenhout, P. Rojo Romeo, P. Regreny, C. Seassal, D. Van Thourhout, S. Verstuyft, L. Di Cioccio, J.-M. Fedeli, C. Lagae, and R. Baets, “Electrically pumped InP-based microdisk lasers integrated with a nanophotonic silicon-on-insulator waveguide circuit,” *Opt. Express* **15**, 6744–6749 (2007).
3. O. Painter, R. K. Lee, A. Yariv, A. Scherer, J. D. O’Brien, P. D. Dapkus, and I. Kim, “Two-dimensional photonic bandgap defect mode laser,” *Science* **284**, 1819–1821 (1999).
4. H. Altug, D. Englund, and J. Vukovic, “Ultrafast photonic crystal nanocavity laser,” *Nat. Phys.* **2**, 484–488 (2006).
5. F. Raineri, A. Yacomotti, T. J. Karle, R. Hostein, R. Braive, A. Beveratos, I. Sagnes, and R. Raj, “Dynamics of band-edge photonic crystal lasers,” *Opt. Express* **17**, 3165–3172 (2009).
6. K. Nozaki, S. Kita, and T. Baba, “Room temperature continuous wave operation and controlled spontaneous emission in ultrasmall photonic crystal nanolaser,” *Opt. Express* **15**, 7506–7514 (2007).
7. C. Monat, C. Seassal, X. Letartre, P. Regreny, P. Rojo-Romeo, and P. Viktorovitch, “InP 2D photonic crystal micro-lasers on silicon wafer: room temperature operation at 1.55  $\mu\text{m}$ ,” *Electron. Lett.* **37**, 764–766 (2001).
8. G. Vecchi, F. Raineri, I. Sagnes, A. Yacomotti, P. Monnier, T. J. Karle, K.-H. Lee, R. Braive, L. Le Gratiet, S. Guilet, G. Beaudoin, A. Talneau, S. Bouchoule, J. A. Levenson, and R. Raj, “Continuous-wave operation of photonic band-edge laser near 1.55  $\mu\text{m}$  on silicon wafer,” *Opt. Express* **15**, 7551–7556 (2007).
9. G. Vecchi, F. Raineri, I. Sagnes, K.-H. Lee, S. Guilet, L. Le Gratiet, F. Van Laere, G. Roelkens, D. Van Thourhout, R. Baets, J. A. Levenson, and R. Raj, “Photonic-crystal surface emitting laser near 1.55 micron on gold-coated silicon wafer,” *Electron. Lett.* **43**, 39–40 (2007).
10. Y. Tanaka, T. Asano, R. Hatsuna, and S. Noda, “Investigation of point-defect cavity formed in two-dimensional photonic crystal slab with one-sided dielectric cladding,” *Appl. Phys. Lett.* **88**, 011112 (2006).
11. Y. Halioua, T. J. Karle, F. Raineri, P. Monnier, I. Sagnes, G. Roelkens, D. Van Thourhout, and R. Raj, “Hybrid InP-based photonic crystal lasers on silicon on insulator wires,” *Appl. Phys. Lett.* **95**, 201119 (2009).
12. T. J. Karle, Y. Halioua, F. Raineri, P. Monnier, R. Braive, L. Le Gratiet, G. Beaudoin, I. Sagnes, G. Roelkens, F. Van Laere, D. Van Thourhout, and R. Raj, “Heterogeneous integration and precise alignment of InP-based photonic crystal lasers to complementary metal-oxide semiconductor fabricated silicon-on-insulator wire waveguides,” *J. Appl. Phys.* **107**, 063103 (2010).
13. J. S. Foresi, P. R. Villeneuve, J. Ferrera, E. R. Thoen, G. Steinmevert, S. Fan, J. D. Joannopoulos, L. C. Kimerling, H. I. Smith, and E. P. Ippen, “Photonic-bandgap microcavities in optical waveguides,” *Nature* **390**, 143–145 (1997).
14. A. R. Md Zain, N. P. Johnson, M. Sorel, and R. M. De La Rue, “Ultra high quality factor one dimensional photonic crystal/photonic wire micro-cavities in silicon-on-insulator (SOI),” *Opt. Express* **16**, 12084–12089 (2008).
15. P. B. Deotare, M. W. McCutcheon, I. W. Frank, M. Khan, and M. Lončar, “High quality factor photonic crystal nanobeam cavities,” *Appl. Phys. Lett.* **94**, 121106 (2009).
16. Y. Zhang, M. Khan, Y. Huang, J.-H. Ryou, P. Deotare, R. Dupuis, and M. Lončar, “Photonic crystal nanobeam lasers,” *Appl. Phys. Lett.* **97**, 051104 (2010).
17. Y. Gong, B. Ellis, G. Shambat, T. Sarmiento, J. S. Harris, and J. Vuckovic, “Nanobeam photonic crystal cavity quantum dot laser,” *Opt. Express* **18**, 8781–8789 (2010).
18. B.-H. Ahn, J.-H. Kang, M.-K. Kim, J.-H. Song, B. Min, K.-S. Kim, and Y.-H. Lee, “One-dimensional parabolic-beam photonic crystal laser,” *Opt. Express* **18**, 5654–5660 (2010).
19. M. Notomi, E. Kuramochi, and H. Taniyama, “Ultrahigh- $Q$  nanocavity with 1D photonic gap,” *Opt. Express* **16**, 11095–11102 (2008).
20. P. Velha, J. C. Rodier, P. Lalanne, J. P. Hugonin, E. Picard, T. Charvolin, and E. Hadji, “Ultra-high-reflectivity photonic-bandgap mirrors in a ridge SOI waveguide,” *New J. Phys.* **8**, 204 (2006).
21. We use FDTD Solutions by Lumerical <http://www.lumerical.com>.
22. J. T. Robinson, C. Manolatos, L. Chen, and M. Lipson, “Ultrasmall mode volumes in dielectric optical microcavities,” *Phys. Rev. Lett.* **95**, 143901 (2005).
23. G. Roelkens, J. Brouckaert, D. Van Thourhout, R. Baets, R. Notzel, and M. Smith, “Adhesive bonding of an InP/InGaAsP dies to processed silicon-on-insulator wafers,” *J. Electrochem. Soc.* **153**, G1015–G1019 (2006).
24. K.-H. Lee, S. Guilet, G. Patriarche, I. Sagnes, and A. Talneau, “Smooth sidewall in InP-based photonic crystal membrane etched by N<sub>2</sub>-based inductive coupled plasma,” *J. Vac. Sci. Technol. B* **26**, 1326–1333 (2008).
25. E. Kapon, *Semiconductor Lasers* (Academic, 1999).
26. G. Bjork and Y. Yamamoto, “Analysis of semiconductor micro-cavity lasers using rate equations,” *IEEE J. Quantum Electron.* **27**, 2386–2396 (1991).